

# Covalent DNA-Encoded Library Workflow Drives Discovery of SARS-CoV-2 Nonstructural Protein Inhibitors

Xudong Wang,<sup>#</sup> Liwei Xiong,<sup>#</sup> Ying Zhu,<sup>#</sup> Sixiu Liu,<sup>#</sup> Wenfeng Zhao, Xinyuan Wu, Mengnisa Seydimemet, Linjie Li, Peiqi Ding, Xian Lin, Jiaxiang Liu, Xuan Wang, Zhiqiang Duan, Weiwei Lu, Yanrui Suo, Mengqing Cui, Jinfeng Yue, Rui Jin, Mingyue Zheng, Yechun Xu, Lianghe Mei,\* Hangchen Hu,\* and Xiaojie Lu\*



Cite This: *J. Am. Chem. Soc.* 2024, 146, 33983–33996



Read Online

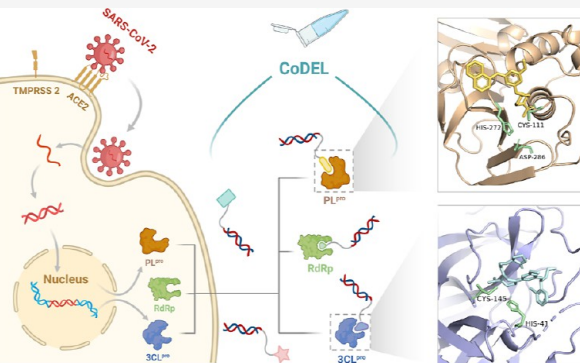
ACCESS |

Metrics & More

Article Recommendations

Supporting Information

**ABSTRACT:** The COVID-19 pandemic, exacerbated by persistent viral mutations, underscored the urgent need for diverse inhibitors targeting multiple viral proteins. In this study, we utilized covalent DNA-encoded libraries to discover innovative triazine-based covalent inhibitors for the 3-chymotrypsin-like protease ( $3\text{CL}^{\text{pro}}$ , Nsp5) and the papain-like protease ( $\text{PL}^{\text{pro}}$ ) domains of Nsp3, as well as novel non-nucleoside covalent inhibitors for the nonstructural protein 12 (Nsp12, RdRp). Optimization through molecular docking and medicinal chemistry led to the development of **LU9**, a nonpeptide  $3\text{CL}^{\text{pro}}$  inhibitor with an  $\text{IC}_{50}$  of  $0.34 \mu\text{M}$ , and **LU10**, whose crystal structure showed a distinct binding mode within the  $3\text{CL}^{\text{pro}}$  active site. The X-ray cocrystal structure of SARS-CoV-2  $\text{PL}^{\text{pro}}$  in complex with **XDS** uncovered a previously unexplored binding site adjacent to the catalytic pocket. Additionally, a non-nucleoside covalent Nsp12 inhibitor **XJS** achieved a potency of  $0.12 \mu\text{M}$  following comprehensive structure–activity relationship analysis and optimization. Molecular dynamics revealed a potential binding mode. These compounds offer valuable chemical probes for target validation and represent promising candidates for the development of SARS-CoV-2 antiviral therapies.



## INTRODUCTION

The novel coronavirus was first identified in late 2019 and subsequently rapidly spread to numerous countries and regions, posing a severe threat to public health due to its high fatality rate and complex clinical manifestations.<sup>1</sup> While vaccines and therapeutic antibodies have proven to be effective in preventing and mitigating COVID-19, their effectiveness has been challenged by the emergence of certain variants of concern, such as the Omicron variant.<sup>2–7</sup>

SARS-CoV-2 is an enveloped, positive-sense, single-stranded RNA virus (Figure 1A).<sup>8–10</sup> The genome sequence exhibits approximately 86% similarity to SARS-CoV and 50% similarity to MERS-CoV, two other members of the betacoronavirus family responsible for previous major outbreaks.<sup>11–13</sup> After entry of SARS-CoV-2 into the host cell, the nuclear envelope and the positive-strand RNA of the virus are released into the cytoplasm.

The open reading frames ORF1a and ORF1b of the positive-strand RNA are translated to generate nonstructural proteins, which are then cleaved by  $\text{PL}^{\text{pro}}$  and  $3\text{CL}^{\text{pro}}$ . This process ultimately produces 16 types of nonstructural proteins, including helicase and RNA-dependent RNA polymerase (RdRp), also known as Nsp12, which participate in viral

transcription and replication processes (Figure 1B).<sup>14–16</sup>  $3\text{CL}^{\text{pro}}$  exhibits a tripartite architecture comprising three distinct structural domains (Figure 1C). Within the well-defined cleft that interconnects structural domain I and structural domain II, a catalytic dyad featuring Cys145 and His41 residues is prominently situated. This catalytic dyad serves as the key determinant responsible for the precise cleavage of pp1a and pp1ab polyproteins, consequently engendering the generation of 12 indispensable functional proteins (Nsp 4–16).<sup>17–19</sup>  $\text{PL}^{\text{pro}}$ , a 35 kDa domain in the 215 kDa multidomain protein Nsp3, is involved in cleaving viral polyproteins pp1a and pp1ab at three sites, generating Nsp1, Nsp2, and Nsp3. It consists of thumb, fingers, and palm subdomains typical of ubiquitin-specific proteases, along with an N-terminal ubiquitin-like domain for substrate recognition

Received: September 18, 2024

Revised: November 13, 2024

Accepted: November 14, 2024

Published: November 22, 2024



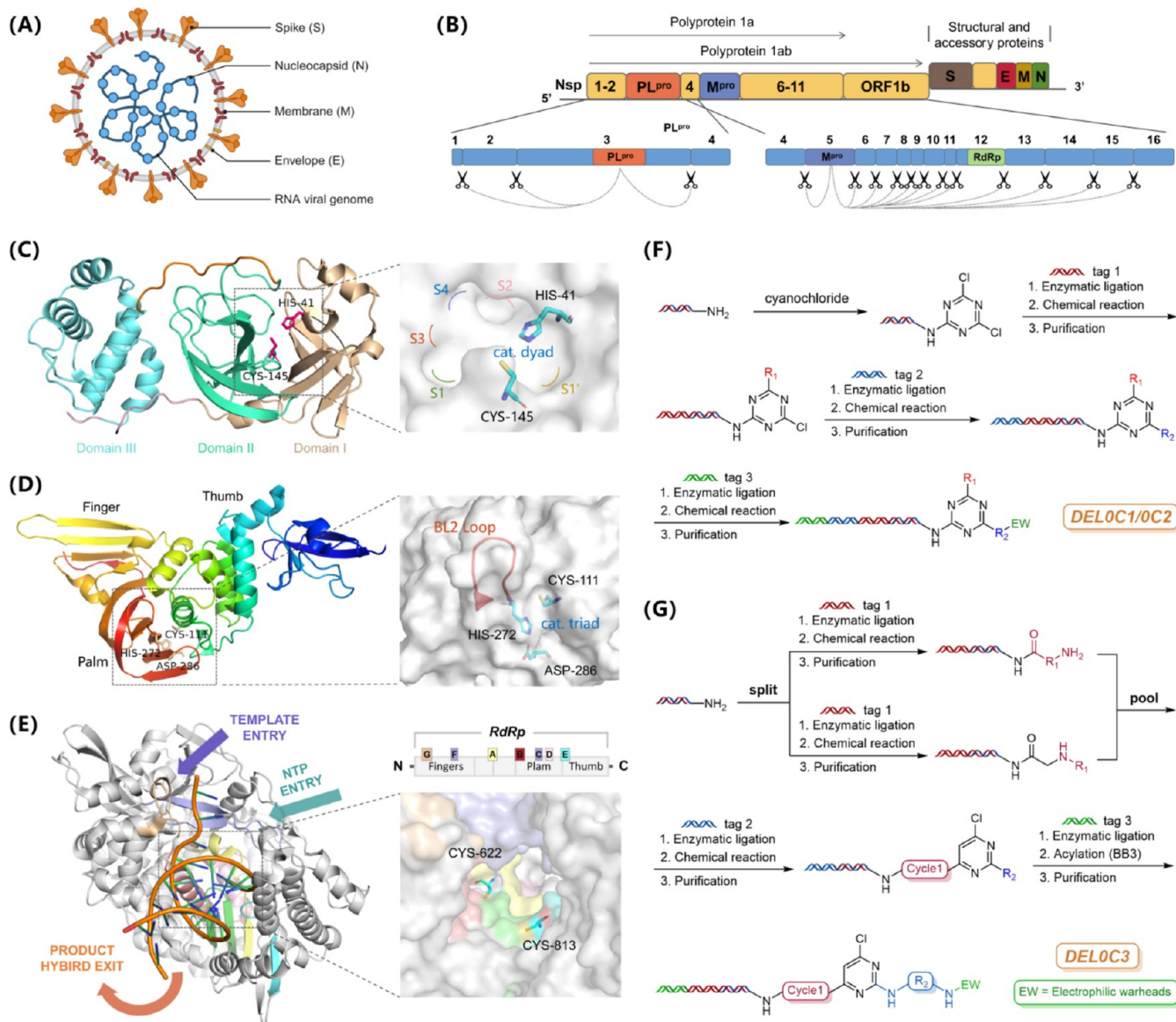


**Figure 1.** (A) Morphological structure and composition of SARS-CoV-2 coronavirus particle. (B) SARS-CoV-2 genes and their expression proteins. (C) Structural diagrams of the 3CL<sub>pro</sub> monomer and its catalytic pocket. (D) Structural diagrams of PL<sub>pro</sub> and its catalytic site. (E) Structural diagrams of Nsp12-RNA complex and the active site for RNA extension. The polymerase motifs are colored as follows: motif A, yellow; motif B, red; motif C and F, purple; motif D, pink; motif E, blue; and motif G, flesh color. (F) Construction route of triazine-based covalent DNA-encoded libraries (DELs), including DEL0C1 and DEL0C2. (G) Construction route of pyrimidine-based covalent DEL, including DEL0C3.

(Figure 1D).<sup>20–22</sup> The catalytic triad comprising Cys111, His272, and Asp286 is located at the thumb–palm interface and is responsible for its enzymatic activity. Nsp 12 contains a right-hand RdRp polymerase domain and a nidovirus-specific N-terminal extension domain that adopts a nidovirus RdRp-associated nucleotidyltransferase (NiRAN) architecture. The polymerase domain and NiRAN domain are connected by an interface domain. The RdRp domain adopts the conserved architecture of the viral polymerase family, comprising three subdomains: fingers, palms, and thumb. The active site, located within the palm subdomain, is formed by the conserved polymerase motifs A to G and is configured similarly to other RNA polymerases (Figure 1E).<sup>23,24</sup>

Multiple peptide-like covalent inhibitors targeting 3CL<sub>pro</sub> have been extensively investigated, demonstrating significant 3CL<sub>pro</sub> inhibitory potency and antiviral activity.<sup>25–30</sup> Nevertheless, these peptidomimetic inhibitors exhibit inherent

drawbacks concerning their low membrane permeability and metabolic stability. An illustrative example is the approved drug paxlovid (PF-07321332) from Pfizer, which necessitates coadministration with ritonavir as a pharmacokinetic booster to address these limitations.<sup>31</sup> Presently, the investigation of PL<sub>pro</sub> binding pockets primarily revolves around those associated with its hydrolytic substrates. Numerous research studies have been dedicated to identifying inhibitors that target this active pocket, with particular emphasis on GRL0617 and its analogues.<sup>32–36</sup> Notably, among these investigations, the incorporation of linkers and electrophilic moieties into GRL0617 led to the development of the first covalent inhibitor.<sup>37</sup> Current research on inhibitors of Nsp12 mainly focuses on nucleoside analogues (NIs), with only a few reports on non-nucleoside analogues (NNIs).<sup>38,39</sup> Furthermore, the scarcity of reported crystallographic structures impedes a comprehensive understanding of the protein's architecture.

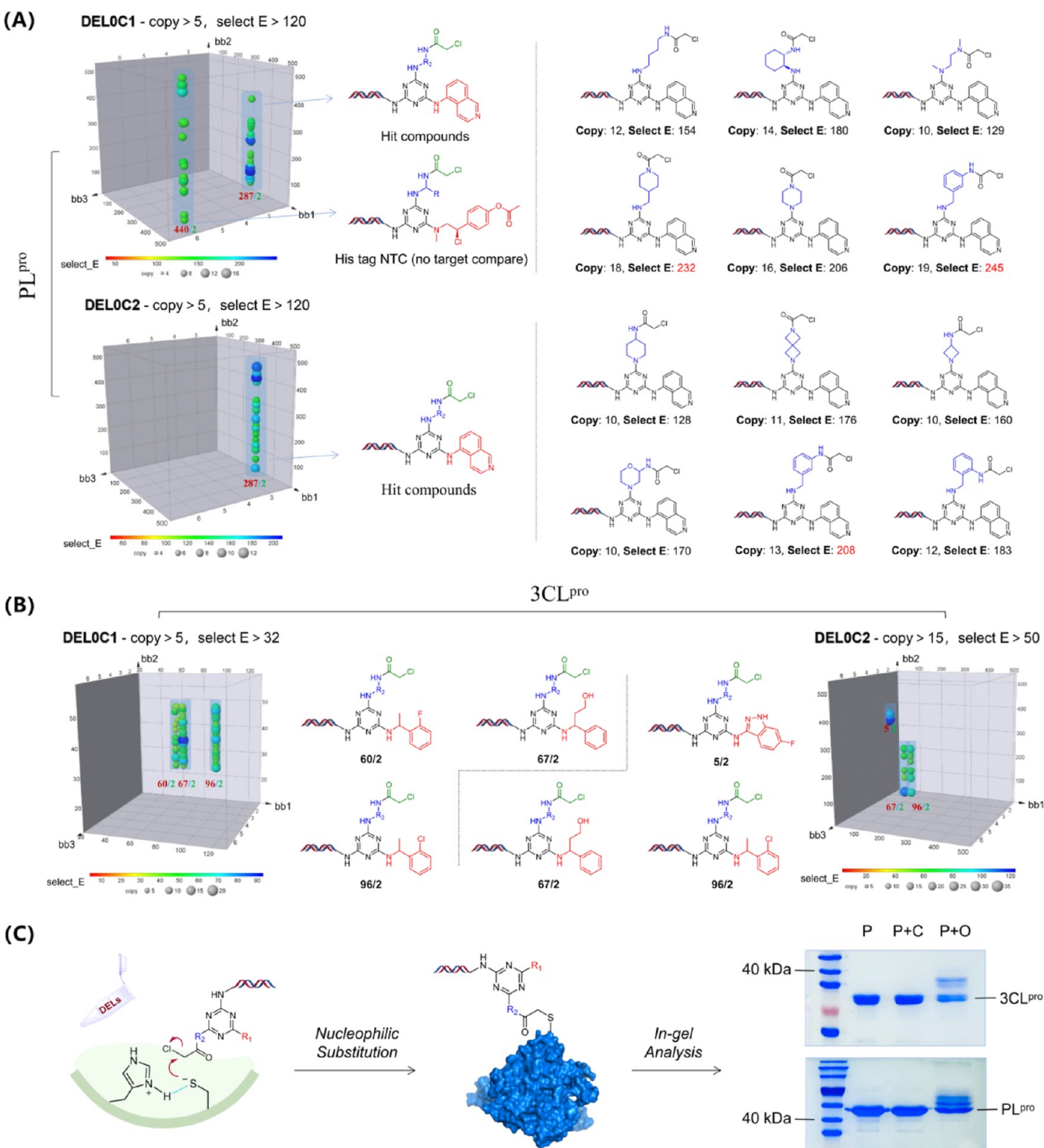


**Figure 2.** Covalent screening profile of DEL0C1 and DEL0C2 against SARS-CoV-2 PL<sup>pro</sup> (A) and 3CL<sup>pro</sup> (B). The selection data have shown the enrichment, copy value, and linear relationship. The copy value in the box represents the number of observed library members. The select E value in the box represents enrichment value of the selected protein against the library of molecules. (C) Mechanism of covalent binding and the workflow of covalent verification. SDS-PAGE analysis stained with Coomassie Brilliant Blue showing protein bands. P represents protein bands, P + C represents protein bands after incubation with on-DNA control compound, and P + O represents protein bands after incubation with on-DNA covalent compounds.

In this paper, we present the inaugural application of covalent DNA-encoded libraries for the identification of covalent inhibitors targeting various SARS-CoV-2 nonstructural proteins (Figure 1F,G). X-ray crystallography elucidates the binding modes of hit molecules obtained through covalent DNA-encoded library (DEL) screening. Notably, crystallo-

graphic analyses of nonpeptidic covalent inhibitors reveal binding hotspots and potential avenues for further optimization in the context of 3CL<sup>pro</sup>. For PL<sup>pro</sup>, crystallographic insights unveil a previously unidentified binding site adjacent to the Cys270 residue, presenting an opportunity for the further development of PL<sup>pro</sup> inhibitors. In addition, we reveal

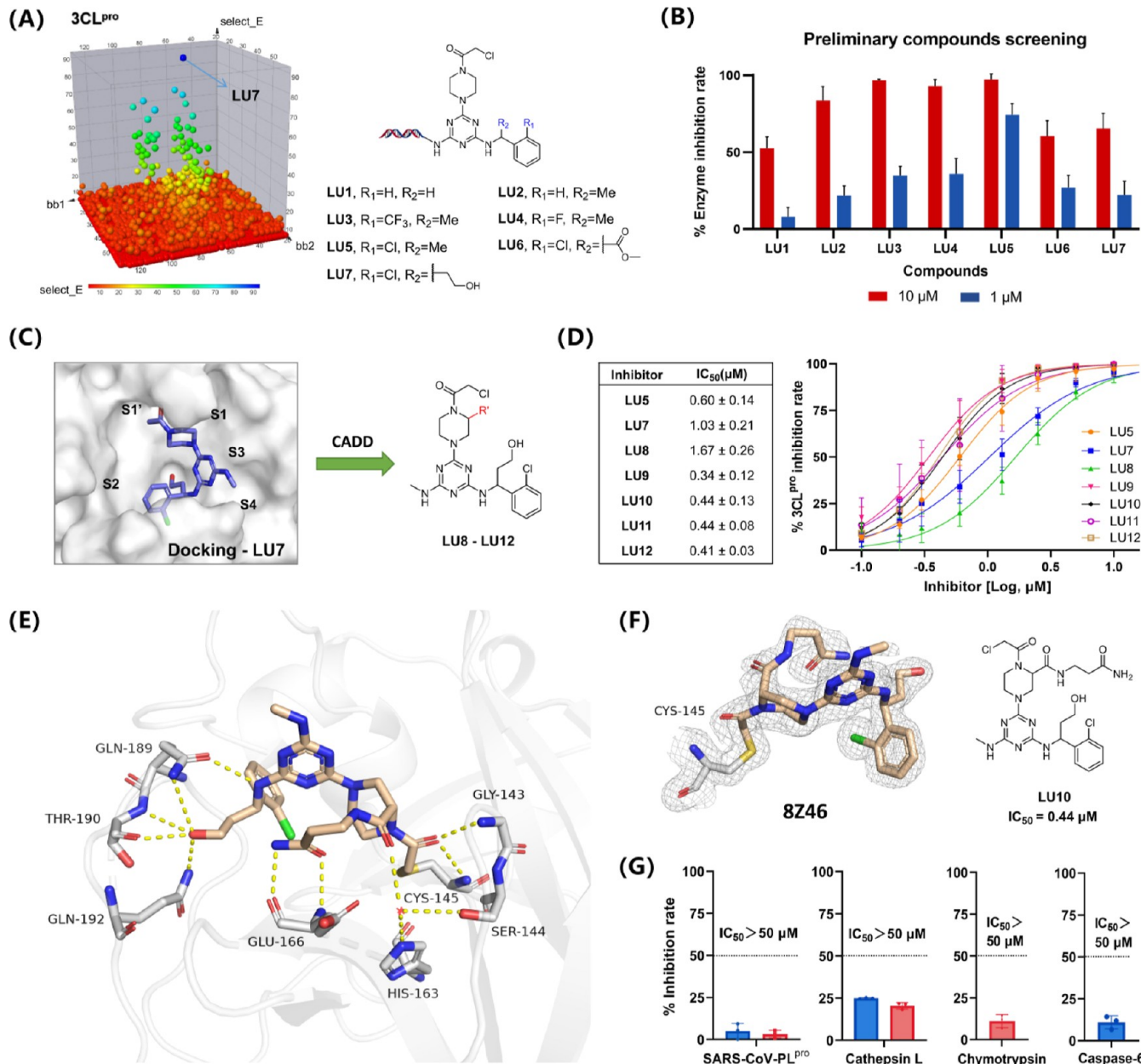


**Figure 3.** (A) The dark blue sphere represents LU7. The structure modification guided by DEL resulted in compounds LU1–LU7. (B) Inhibition rates of LU1–LU7 on 3CL<sup>pro</sup> enzyme at concentrations of 1 and 10  $\mu$ M. (C) Compounds LU8–LU12 obtained via computer-assisted drug design (SBDD) through the modification of compound LU7. (D) Dose–response curves for the inhibition of SARS-CoV-2 3CL<sup>pro</sup>. The table indicates the corresponding IC<sub>50</sub> values. (E) X-ray crystal structure of SARS-CoV-2 3CL<sup>pro</sup> in complex with LU10 (parchment). (F) 2Fo – Fc electron density map, shown in gray, is contoured at 1 $\sigma$ . (G) Target selectivity of SARS-CoV-2 3CL<sup>pro</sup> inhibitors against host proteases. Red bars indicate 20  $\mu$ M, while blue bars indicate 50  $\mu$ M.

a non-nucleoside covalent inhibitor targeting Nsp12 and elucidate its potential covalent binding site through molecular dynamics (MD).

## RESULTS AND DISCUSSION

**Covalent Screening of Triazine-Based DNA-Encoded Libraries for PL<sup>pro</sup>/3CL<sup>pro</sup> Inhibitors.** Novel covalent inhibitors were identified through the screening of covalent DNA-encoded libraries based on the triazine scaffold (Figure 1F). Within this framework, trichlorotriazine serves as the trifunctional group scaffold, widely employed in library construction and DEL screening to derive a series of lead compounds.<sup>40–43</sup> In the pursuit of targets 3CL<sup>pro</sup> and PL<sup>pro</sup>, we

initially employed a diverse set of noncovalent DELs for screening. However, the desired outcomes were not attained (Table S6). Consequently, through the introduction of electrophilic warheads into intermediated libraries, we established two covalent compound libraries, namely, DEL0C1 and DEL0C2 (Figure S1). The difference between these two libraries lies in the types and quantities of building blocks in the second cycle. To assess the screening outcomes, it is imperative to establish cutoff values for both libraries to mitigate background noise interference.<sup>44</sup> Focusing on the PL<sup>pro</sup> target, we set the copy value threshold for both libraries to exceed 5, with an enrichment criterion surpassing 120 (Figure S3). With this setting, we can clearly visualize the

enrichment trends in the three-dimensional plots. The screening results reveal that DEL0C1 and DEL0C2 demonstrate selectivity solely toward the 5-aminoisoquinoline fragment in cycle 1 (Figure 2A). Concerning the fragments employed in the libraries construction process during cycle 2, both libraries demonstrate differential levels of enrichment toward various types of diamine structures (Table S7). This observation implies that, during the actual covalent binding process, the cycle 2 fragment functions solely as a linker in ligand association. Upon analyzing the enrichment results, it is evident that the L9 and B8 fragments exhibit the highest degree of enrichment in the screening of both libraries (Table S7). Specifically, the select *E* values for L9 and B8 in DEL0C1 and DEL0C2 are 245 and 208, respectively. Furthermore, regarding the electrophilic fragment in cycle 3, both DEL0C1 and DEL0C2 screening results demonstrate specificity toward chloroacetamide (Figure 2A).

Regarding the 3CL target, while its screening results similarly exhibit linear enrichment in the three-dimensional plot (Figure 2B), these linearly related points represent an identical reaction building block. This occurrence stems from the fact that during library construction, each reaction building block in cycle 2 is encoded by multiple distinct tags (Tables S1 and S2). From the encoded structural information, it is evident that these identical building blocks all feature piperazine structures. This observation suggests the critical role of the piperazine ring in maintaining conformation during the covalent binding process. Experimental results validating this hypothesis were obtained through ring-opening of the linker and scaffold hopping (Figure S10). The screening results from cycle 1 reveal enrichment toward a class of structurally similar building blocks containing benzylamine moieties (Figure 2B). Furthermore, these structures exhibit versatility at the benzyl position, allowing for diverse substitutions or derivatizations, such as methyl introduction, hydroxylation, and cyclization. These outcomes offer clear directions for subsequent derivatization efforts. For the electrophilic segment in cycle 3, screening results from DEL0C1 and DEL0C2 align with those of the PL<sup>pro</sup> target screening, indicating specificity toward chloroacetamide.

Compared to conventional DEL affinity screening,<sup>45–47</sup> covalent screening involves repetitive denaturation and elution steps during the screening process to ensure the subsequent identification of covalently bound molecules. However, this process cannot guarantee the complete removal of all noncovalently bound molecules. Therefore, covalent binding validation is imperative to ascertain the occurrence of covalent interactions among the screened molecules and to precisely identify the covalent binding sites. Our previous research findings indicate that the PL<sup>pro</sup> Cys270 residue represents a potential covalent binding residue,<sup>48,49</sup> marking the first report of a small-molecule inhibitor covalently targeting residue Cys270. Hence, our primary objective concerning covalent molecules derived from covalent DEL screening is to delineate their covalent binding sites. To achieve this, we conducted a comparative screening using the PL C111S mutant protein to screen DEL0C1 and DEL0C2. The screening outcomes revealed no discernible enrichment of molecules in either library upon the introduction of the catalytic site cysteine mutation (Figure S4). This suggests that the site of covalent binding between molecules in covalent DEL and wild-type PL<sup>pro</sup> is the Cys111 residue. Subsequently, we employed gel electrophoresis for on-DNA covalent binding validation of

these two coronaviral polyproteins. Initially, covalent molecules with DNA chains (Schemes S1 and S2) and on-DNA control compound (Scheme S4) were synthesized, and the procedure outlined in Figure 2C was used for in-gel analysis of PL<sup>pro</sup> and 3CL<sup>pro</sup> targets. SDS-PAGE analysis demonstrated that hit molecules directly obtained from screening exhibited covalent binding activity (Figure 2C).

#### Hits Resynthesis and Evaluation of 3CL<sup>pro</sup> Inhibition.

Based on the analysis of DEL screening results, it is evident that positions R1 and R2 emerge as potential sites for modification or derivatization. Consequently, our investigation initially focused on positions R1 and R2, leading to the synthesis of compounds LU1–LU7 (Figure 3A). Notably, compounds LU4, LU5, and LU7 were directly identified through screening, with LU7 displaying significant enrichment in both libraries (Figures 3A and S5). We conducted separate tests to evaluate the inhibitory effects of these seven compounds on the activity of SARS-CoV-2 3CL<sup>pro</sup> at concentrations of 1 and 10 μM (Figure 3B). Our results revealed that both LU5 and LU7 exhibited significant inhibition at 1 μM. Considering the superior enrichment of LU7 indicated by DEL affinity screening, implying its stronger binding affinity to the protein, we proceeded to further investigate LU7 as our primary compound of interest.

As proteins are rich in cysteine, the majority of cysteine residues are situated internally within the protein structure with only Cys145 and Cys44 potentially exposed as reactive cysteines at the catalytic pocket (Figure S6). However, the reported covalent inhibitors of 3CL<sup>pro</sup> predominantly target the catalytic Cys145.<sup>50–54</sup> Consequently, we conducted covalent molecular docking of compound LU7 with this binding site (Figure 3C). The covalent docking results reveal the existence of two potential binding modes, wherein a conformational flip of the small molecule occurs contingent upon the positioning of the methylamine moiety (Figure S7A,B). These dual outcomes afford a comprehensive elucidation concerning the binding of both small molecules and proteins. Nevertheless, DEL screening unequivocally establishes that the DNA tethering site must reside within the solvent-exposed region to enable conjugation. Consequently, the covalent docking outcomes, wherein the methylamine moiety extends toward the solvent-accessible domain, carry greater scientific merit (Figure S7A). The docking results reveal that the amide carbonyl group of the covalent linker can establish hydrogen bonding interactions with the amide nitrogen atom of Gly143, whereas the hydroxyl group introduced by the benzyl moiety of BB1 (building block 1) can engage in robust hydrogen bonding interactions with the amide carbonyl of His164 (Figure S7C). This observation underscores a potentially pivotal factor governing the binding affinity between LU7 and 3CL<sup>pro</sup>. Considering further molecular optimization, we observe that the S1 site exhibits considerable unoccupied space. Upon overlaying complexes of some previously reported 3CL<sup>pro</sup> inhibitors, we find that fragments binding to the S1 site predominantly adopt a γ-butyrolactam structure, establishing multiple hydrogen-bonding interactions with His163 and Glu166 (Figure S8). In light of this, we introduced analogous structures into the molecular framework to synthesize compounds LU8–LU12. Subsequent testing of the IC<sub>50</sub> values of these compounds revealed a significant enhancement in the inhibitory activity upon incorporation of this structure (Figure 3D). This underscores the potential of derivatives on the piperazine ring as an

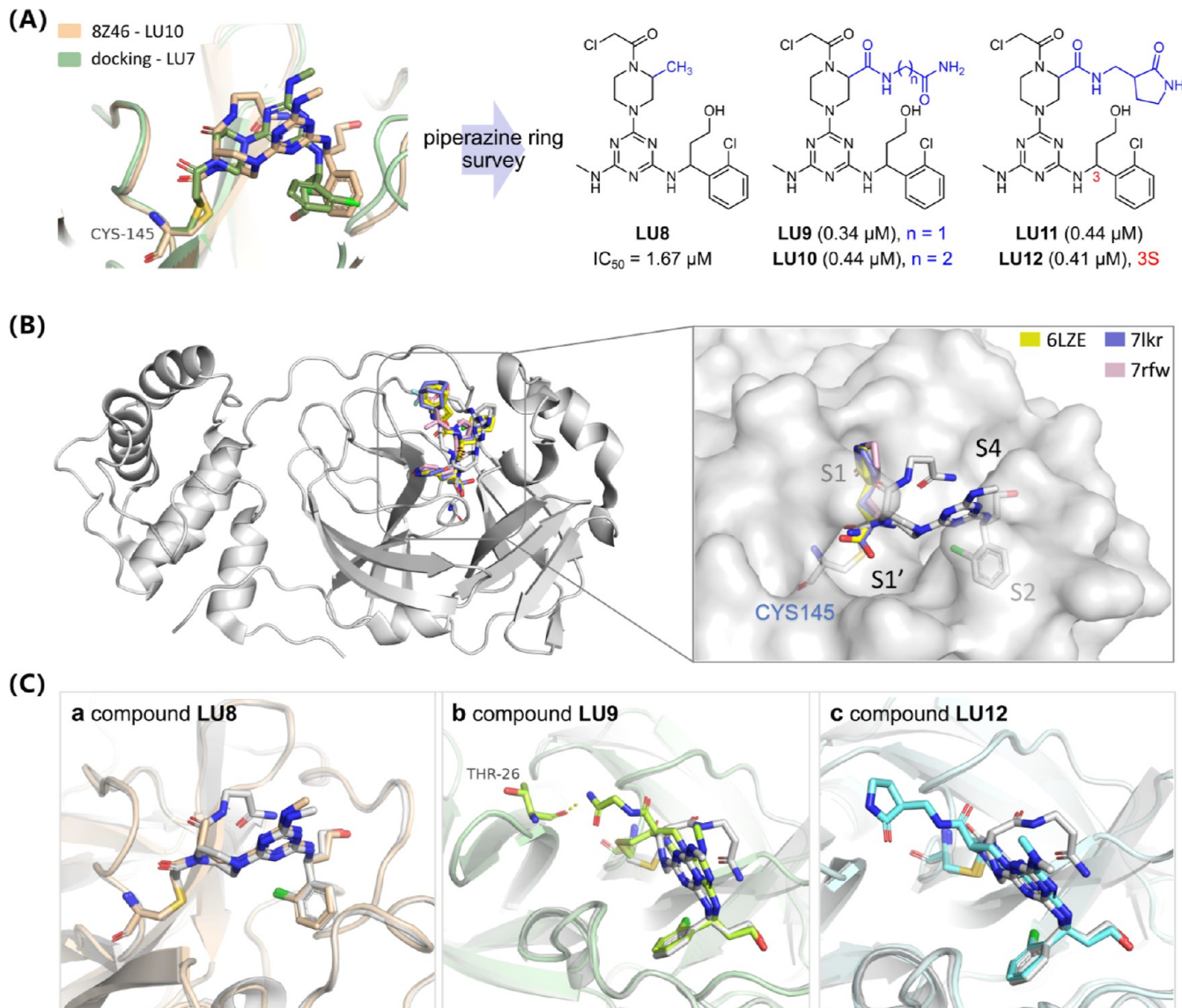


**Figure 4.** (A) Superposition of crystal structure of LU10 (parchment) and docking structure of LU7 (moss) and the structure of LU8–LU12 along with their corresponding  $IC_{50}$  values. The red text indicates that the absolute configuration at the 3' position of LU12 has been determined. (B) Superposition of crystal structure of LU10 (gray) and  $\gamma$ -butyrolactam structures. For clearer visualization, displaying only the structural fragment of  $\gamma$ -butyrolactam. (C) Superposition of crystal structure of LU10 (gray) and docking structure of LU8 (coconut), LU9 (lime), LU12 (blue).

alternative promising modification site. In conclusion, the selectivity of compound LU12 against several representative human proteins was assessed. The findings indicated values exceeding 50  $\mu M$  across all of the evaluated human proteins (Figure 3G).

**X-ray Crystal Structures of SARS-CoV-2 3CL<sup>pro</sup> in Complex with LU10.** Based on the active compound LU10, we elucidated its cocrystal structure with 3CL<sup>pro</sup> (Figure 3E). The cocrystal structure reveals that LU10 covalently binds to the catalytic site at Cys145. The triazole ring acts as a scaffold in the structure, linking the active moiety, covalent linker, and DNA. The crystal structure shows that the active fragment occupies the S2 and S4 sites, and the hydroxyl group derived from the R2 moiety forms multiple hydrogen bonds with Gln189, Thr190, and Gln192, constituting a hydrogen bond network. The nitrogen atom connecting the active moiety also participates in hydrogen bonding with Gln189. The side chain derived from the piperazine ring binds at a position different

from that of the reported  $\gamma$ -butyrolactam binding site (Figure 4B). Under the tension exerted by the piperazine ring, the derived angle deviates, extending toward the middle portion between the S1 and S4 sites and forming hydrogen bonds with the nearby Glu166. Further molecular docking simulations demonstrated that when the side chain was methylated in compound LU8, its methyl-derived direction aligned well with that of LU10. Extending the side chain to compounds LU9 and LU12 resulted in a deviation in the derived direction toward the S1' pocket, indicating potential influences of side chain length and the conformation of carbon atoms bound to the side chain on the binding mode (Figure 4C). In the crystal structure of this complex, a nonconserved water molecule forms hydrogen bond networks with Ser144, His163, and the carbonyl groups of piperazine side chains, further stabilizing the conformation of the piperazine ring. The amide carbonyl group at the covalent binding site interacts via hydrogen bonding with Gly143 and Cys146.

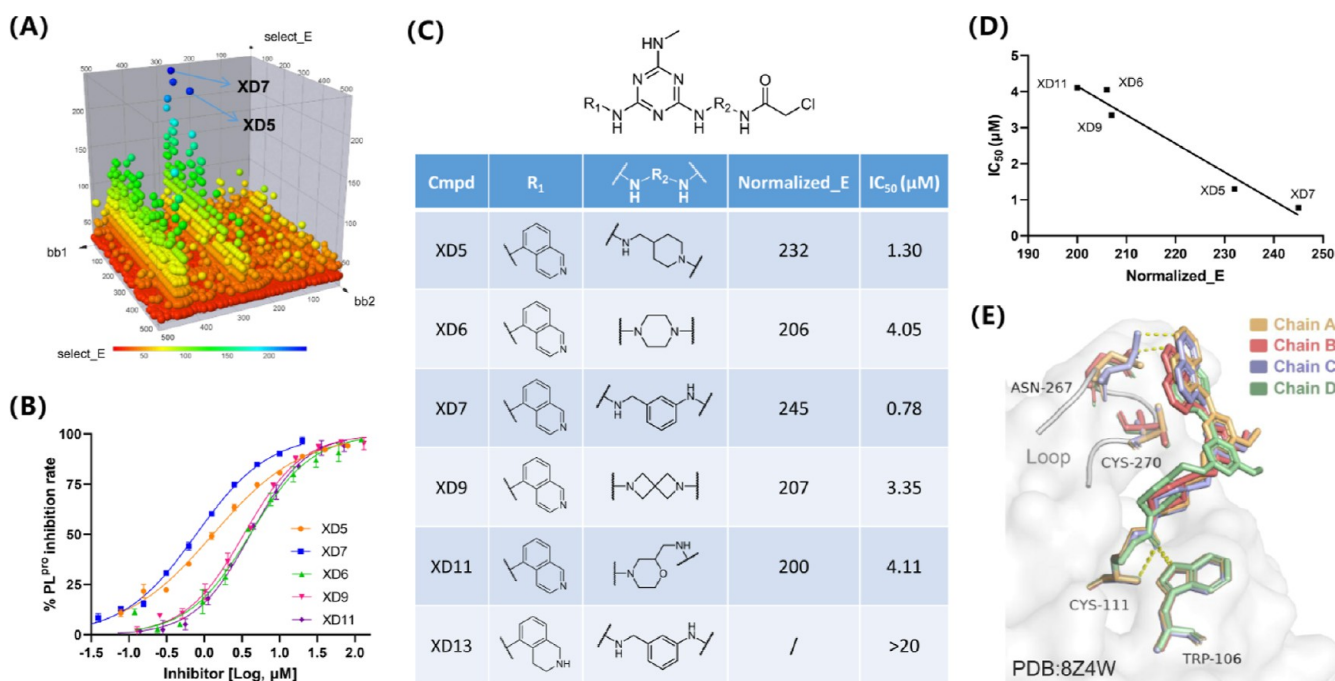


**Figure 5.** (A) Three-dimensional screening structure of PL<sup>pro</sup>, where the vertical axis represents enrichment. (B) Dose–response curves for the inhibition of SARS-CoV2 PL<sup>pro</sup>. (C) Compound structures along with normalized *E* values and IC<sub>50</sub> values. (D) Relationship between normalized *E* values and IC<sub>50</sub> values. (E) X-ray crystal structure of SARS-CoV-2 PL<sup>pro</sup> in complex with XD5.

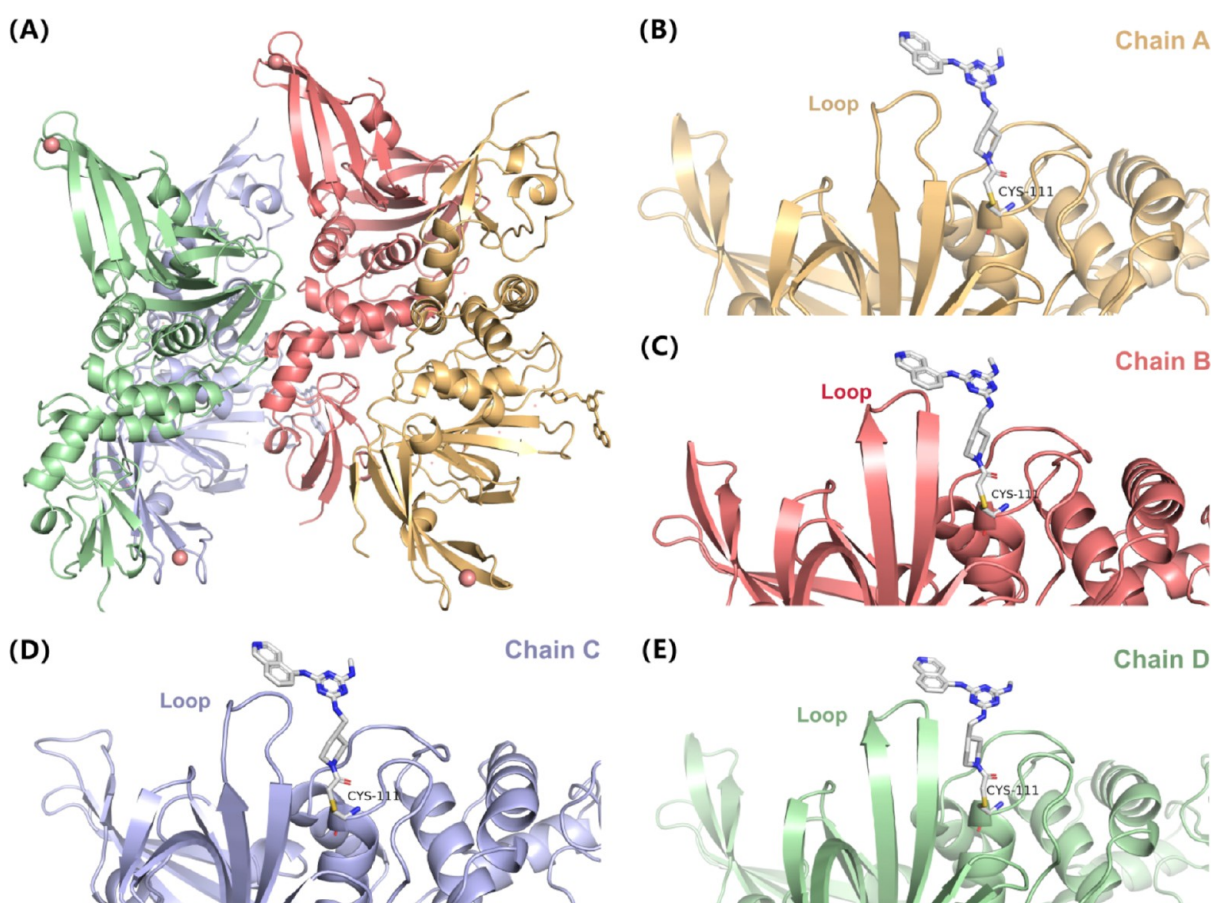
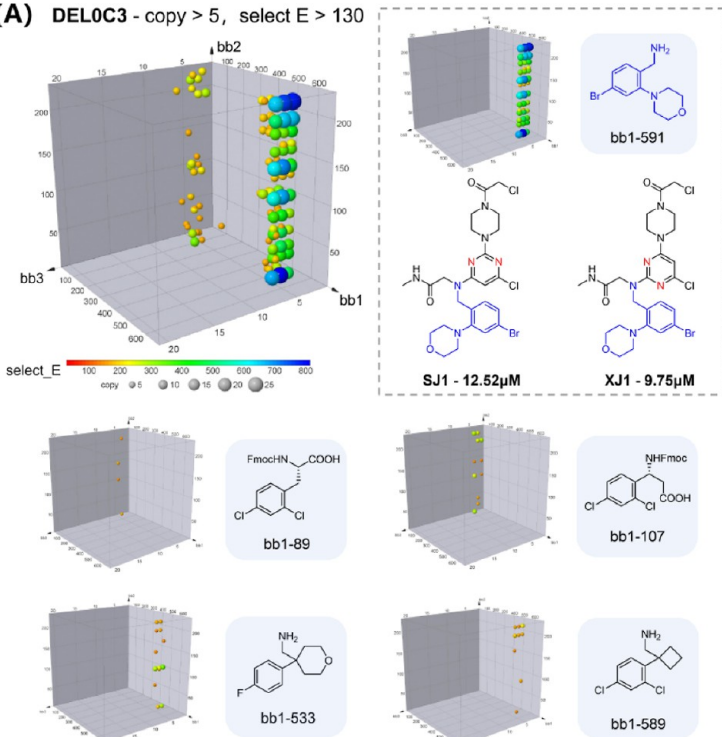


**Figure 6.** Determination of the cocrystal structure of the SARS-CoV-2 PL<sup>pro</sup>-XD5 (PDB: 8Z4W). (A) Cartoon structures of the binding pockets of XD5 and the depiction of four monomers in an asymmetric unit. The crystal structure displays a shallow surface binding site near the catalytic pocket where the compound binds, and similar binding modes are observed in different monomers, such as (B–E).

## (A) DEL0C3 - copy &gt; 5, select E &gt; 130

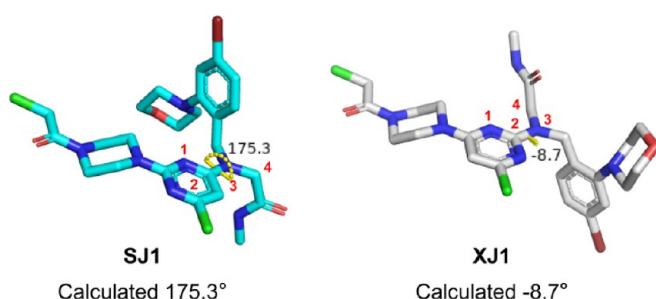


## (B)

Chemical structure of compound XJ1: BrC1=CC=C(C=C1N2C(N3CCCC3)C(=O)N(C4=CC(F)=CC=C4)C2=O)N3CCCC3

Cmpd	R1	R2	R3	R4	$IC_{50} (\mu M)$
XJ1	6-Cl		morpholinyl	Br	9.75
XJ2	5-NO <sub>2</sub>		morpholinyl	Br	1.37
XJ3	5-Me 6-Cl		morpholinyl	Br	> 10
XJ4	6-Cl		morpholinyl	Br	0.44
XJ5	6-Cl		morpholinyl	Br	0.12
XJ6	6-Cl	ethyl	morpholinyl	Br	0.38
XJ7	6-Cl	methyl	morpholinyl	Br	0.39
XJ8	6-Cl	H	morpholinyl	Br	0.60
XJ9	6-Cl	H	Cl	Br	N.D.
XJ10	6-Cl	H	Cl	Cl	N.D.
XJ11	6-Cl	H	Cl	F	N.D.
XJ12	6-Cl	H	Cl	CF <sub>3</sub>	> 10
XJ13	H	H	morpholinyl	Br	0.82
XJ14	H	H	Cl	Br	1.79
XJ15	H	H	Cl	Cl	1.71
XJ16	H	H	Cl	F	> 10

## (C)



## (D)

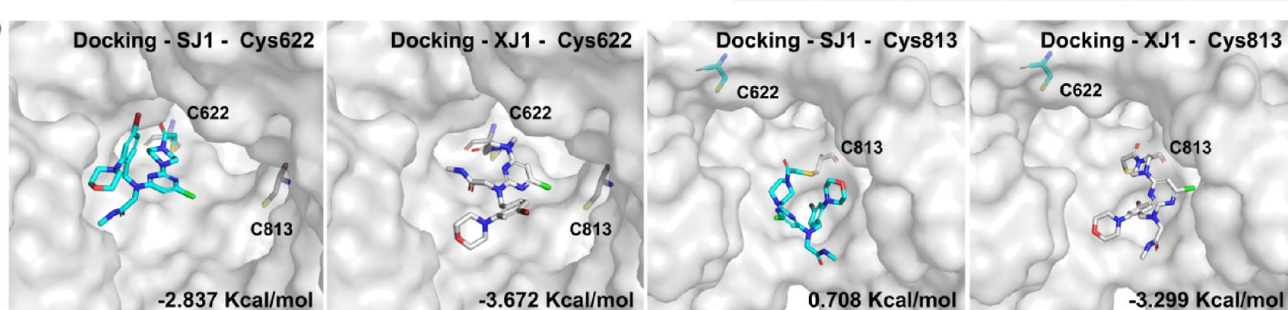


**Figure 7.** (A) Covalent screening profile of DEL0C3 against the SARS-CoV-2 Nsp7/8/12 complex. SJ1 and XJ1 are hit compounds directly screened and validated from DEL0C3. (B) Exploration of potential modification sites on compound XJ1 based on SAR data from DEL0C3 screening. (C) Energy minimization and frequency analysis results obtained using Gaussian 16 software, with calculations performed at the B3LYP/6-311G\*\* level of theory and solvent effects simulated using the conductor-like polarizable continuum model (CPCM). (D) Surface structures of the covalent docking of SJ1 and XJ1 with Cys622 and Cys813, respectively.

**Hits Resynthesis and Evaluation of PL<sup>Pro</sup> Inhibition.**

The ultimate library architectures of DEL0C1 and DEL0C2 exhibit similarities (Figure 1F), albeit with minor discrepancies in the reagents utilized during each library synthesis round (Tables S1 and S2). Considering the nonspecific enrichment observed for cycle 2, namely, the linker portion, in both libraries, a comparative analysis of the enrichment levels of structure XD7, obtained from screening in both libraries

(Figure 2A), was conducted. The select *E* values representing XD7 in different libraries were normalized (Figure 5C), facilitating the integration of the screening outcomes from the two libraries. We established a standardized *E* value cutoff of 200, resulting in the identification of five compounds, XD5, XD6, XD7, XD9, and XD11 that met the structural criteria. Subsequently, we evaluated the  $IC_{50}$  values of these compounds. Our findings revealed a linear correlation between

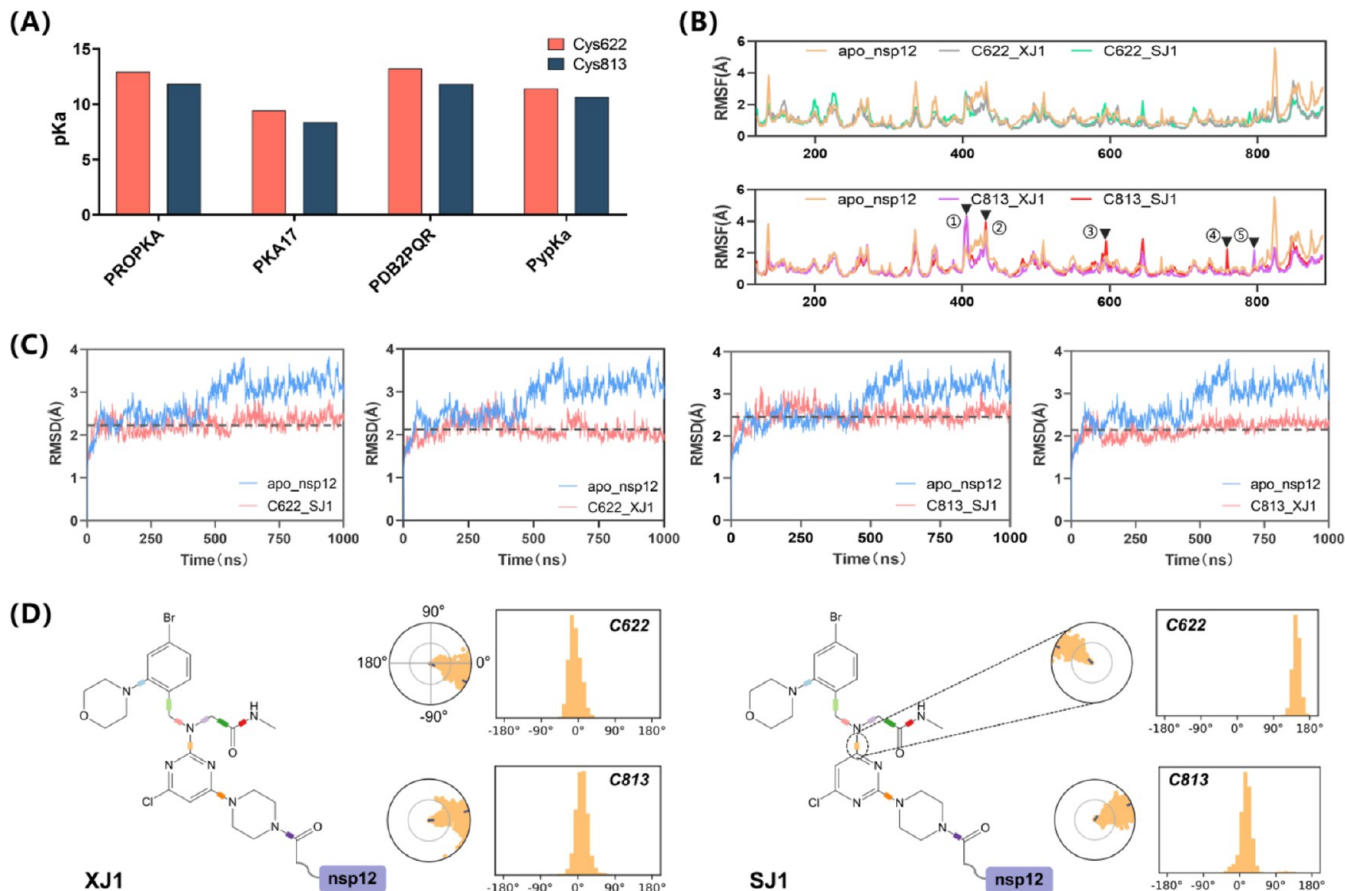


**Figure 8.** (A) Predictive  $pK_a$  values for Cys622 and Cys813 in Nsp12 using traditional single-structure-based  $pK_a$  methods. (B) Stacked line plot of amino acid root-mean-square fluctuations (rmsf) under covalent ligand interactions and without covalent ligands. (C) Root mean square deviation (rmsd) plots of Nsp12, which contain nonstandard residue (C622\_SJ1, C622\_XJ1, C813\_SJ1, C813\_XJ1) and 100 ns of the protein backbone. The blue line represents the rmsd of apo\_Nsp12 (the ligand-free form of Nsp12), while the pink line represents the rmsd of the Nsp12-ligand complex. (D) Covalent ligand torsion profiles for SJ1 and XJ1. Docked ligands with different color codes correspond to the torsion plots.

the standardized  $E$  values and the  $IC_{50}$  activity (Figure 5D). Consequently, we were able to quantify the outcomes of the affinity screening, thereby providing a more comprehensive understanding of the DEL screening results. Unlike the screening outcomes observed for 3CL<sup>pro</sup>, PL<sup>pro</sup> screening against DEL0C1 and DELOC2 consistently demonstrated selectivity toward the 5-aminoisoquinoline fragment within BB1. Given the limited structural diversity within the library (Figure S10), we pursued diverse substitutions of quinoline and isoquinoline structures in cycle 1. However, these compounds exhibited modest PL<sup>pro</sup> inhibition activity (Table S8). Furthermore, dearomatization of the isoquinoline structure to yield compound XD13 resulted in a noticeable activity decrease compared to XD7. These findings collectively underscore the indispensable activity of the 5-aminoisoquinoline fragment within the compounds, significantly contributing to their overall activity. Nonetheless, exploring 5-aminoisoquinoline with different substituents remains an intriguing avenue for future research. In the context of cycle 2, our previous analysis indicates that the structural segments in this region primarily serve as linkers in protein interactions. Subsequently, we synthesized structures exhibiting high enrichment within the library (Figure 5C and Table S7). Through the comparison of normalized  $E$  values and activity analyses, it becomes apparent that compounds such as XD5 and XD7, featuring nucleophilic substitution occurring at one

end of the triazine moiety connected to a methylene group, manifest favorable activity profiles. This observation suggests that the increased flexibility of the N atom proximal to the triazine moiety and its associated C atom may enhance the overall molecular binding to the protein. Furthermore, the removal of the electrophilic warhead portion from the structure results in diminished compound activity (Table S8).

**X-ray Crystal Structures of SARS-CoV-2 PL<sup>pro</sup> in Complex with XD5.** To gain a deeper understanding of the precise ligand binding mode, a crystal structure of SARS-CoV-2 PL<sup>pro</sup> in complex with XD5 was determined at a resolution of 2.3 Å (PDB: 8Z4W). As anticipated, the contiguous electron density is clearly visible between C111 and the acetyl group, confirming the formation of a covalent bond between the protease and XD5 (Figure 5E). The asymmetric unit is composed of four SARS-CoV-2 PL<sup>pro</sup> monomers (Figure 6A). Across diverse monomers, the compound distinctly forms covalent bonds with a superficial binding site proximal to the catalytic pocket of SARS-CoV-2 PL<sup>pro</sup>. In all chains, the acetyl group of XD5 establishes two hydrogen bonds (H-bonds) with Cys111 and Trp106. Specifically, in both chain B and chain D, the compound's quinoline moiety was observed to form an additional hydrogen bond with Asn267, which is located on the loop region of the protein (Figure 6B,D). This interaction likely served as a pivotal determinant of the activity attributed to the quinoline moiety. Furthermore, the apparent proximity

of Cys270 on the loop region to the XDS structure provided a structural rationale for subsequent compound design aimed at covalent binding to Cys270.

### Covalent Screening and Hit Resynthesis of Nsp12.

The successful identification of Nsp12 covalent inhibitors was achieved using a pyrimidine-based covalent DEL (Figure 1G). Nsp7 and Nsp8 have been reported as cofactors involved in the formation of the RNA polymerase complex that mediates RNA replication.<sup>55</sup> Therefore, we employed the Nsp7/8/12 complex as the screening target for DEL0C3. Furthermore, SDS-PAGE confirmed that the screened on-DNA hit compounds exhibit direct covalent interactions with Nsp12 (Figure S12).

The screening results for Nsp12 are analogous to those observed for the PL<sup>pro</sup> target. Since identical reactive building blocks are encoded by distinct tags, the observed enrichment profiles actually correspond to the same structural entities (Figure 7A). Among these, bb1–S19, which exhibited the highest level of enrichment, was prioritized for synthesis and validation. However, considering the selectivity of the trichloropyrimidine reaction site during library construction (Figure S1C), we synthesized both SJ1 and XJ1 and evaluated their inhibitory activities. The IC<sub>50</sub> values were tested to be 12.52 and 9.75 μM, respectively. Based on the screening results and analysis of reactive building blocks with varying enrichment levels, we identified that the bromine and morpholino groups in the bb1–S19 structure could be replaced with other halogens. Additionally, the trichloropyrimidine core and nucleic acid linkage positions were identified as suitable sites for intrinsic modifications. Accordingly, we synthesized compounds XJ2 through XJ16 with various modifications and tested their IC<sub>50</sub> values (Figure S13). The activity results for XJ1–XJ3 and XJ13–XJ16 indicate that modifications to the core structure do not significantly impact the inhibitory activity. Conversely, compounds XJ4–XJ8 show a substantial enhancement in activity when hydrophilic groups are introduced at the nucleic acid linkage position, with XJ5 achieving an IC<sub>50</sub> value of 0.12 μM. Furthermore, compounds XJ9–XJ12 exhibit a significant decrease in activity when both the nucleic acid site and the morpholino group are substituted, which aligns with the structure–activity relationship (SAR) observed in the DEL0C3 screening results.

**Covalent Docking and MD Simulation Study.** To further elucidate the covalent binding sites of hit compounds, quantum mechanics/molecular mechanics (QM/MM) analysis is essential. We performed quantum mechanical calculations on SJ1 and XJ1 using Gaussian 16 software, applying the Conductor-like Polarizable Continuum Model (CPCM) with the opt + freq method. The optimization results reveal a 184° dihedral angle difference between atoms 1–4 in SJ1 and XJ1 (Figures 7C and S11), indicating rotation between the nucleic acid linkage position and piperazine ring. Given that both SJ1 and XJ1 possess covalent binding capabilities, we speculate that the lowest energy conformation of SJ1 might undergo a transition into XJ1 during dynamic binding processes. Subsequently, we conducted semiflexible covalent docking of SJ1 and XJ1 with Cys622 and Cys813, respectively, both of which are located within the active pocket (Figure 7D). Since the hit compound is a NNI, RNA was excluded from the docking simulations. The docking centers were instead focused on the covalent amino acid residues to accurately model binding interactions under physiological pH conditions. The docking scores for SJ1 and XJ1 covalently docked with Cys622

were −2.837 and −3.672 kcal/mol, respectively, whereas the docking scores with Cys813 were 0.708 and −3.299 kcal/mol, respectively. The docking results indicate that the system exhibits lower energy and greater stability when covalently interacting with the Cys622 residue. Additionally, we employed several single-structure-based pK<sub>a</sub> prediction tools to estimate the pK<sub>a</sub> values of all cysteine residues in Nsp12 (Table S12).<sup>56</sup> The results showed that all four prediction tools estimated the pK<sub>a</sub> of Cys622 to be higher than that of Cys813 (Figure 8A).

Furthermore, to support the docking analysis, we conducted an MD simulation study using the DESMOND module from D. E. Shaw Research. The solvation of the docked complex was performed using the SPC solvent model within a cubic box with a 10 Å spacing. Neutralization of the solvated system was achieved by adding counterions. All systems were equilibrated for 100 ns at 300 K and 1.013 atm.<sup>57,58</sup> We plotted the rmsd of the protein backbone over time for four covalent binding modes (Figure 8C). The results indicate that all four covalent modes reached a stable state after 500 ns of simulation. Notably, the rmsd of Nsp12 backbone covalently bound to SJ1 and XJ1 at the Cys622 residue was lower, indicating that the protein exhibits smaller fluctuations and greater stability at this nonstandard residue during the dynamic simulation. Additionally, we analyzed the rmsf of each amino acid under the four binding modes (Figure 8B). The results show that the fluctuations of amino acids in the protein covalently bound to Cys622 are relatively smaller compared to those in apo\_nsp12, suggesting that this covalent binding increased stability. In contrast, the protein covalently bound at Cys813 exhibits pronounced fluctuations in several amino acids, suggesting that covalent attachment at this site may contribute to the instability. Previous QM analysis indicated that SJ1 and XJ1 have the potential to interconvert between their lowest energy conformations. Therefore, we further analyzed the ligand torsion during the simulation process (Figure 8D). The results show that following the covalent binding of SJ1 to the protein at Cys622, subsequent dynamics simulations reveal torsional rotations, with the rotation angles primarily clustering around 180°. This observation is consistent with the findings from the QM analysis. In addition, we conducted a comprehensive assessment of the drug-like properties of the compounds obtained through DEL screening or optimization, including their adherence to Lipinski's rule of five, to evaluate their potential as viable drug candidates (Table S13).

## CONCLUSIONS

In summary, our study introduces a methodology for discovering covalent inhibitors targeting key proteins of SARS-CoV-2. In this study, we successfully identified hit compounds targeting various SARS-CoV-2 nonstructural proteins, including Nsp3, Nsp5, and Nsp12. It should be noted that current inhibitors targeting nonstructural proteins exhibit limited structural diversity and mechanisms of action. For example, the marketed inhibitors for 3CL<sup>pro</sup> are primarily peptide-like inhibitors,<sup>59,60</sup> while marketed inhibitors for RdRp are all NIs.<sup>61,62</sup> As such, we are interested in developing inhibitors with novel structures. DEL technology, as a high-throughput screening method, combined with the covalent binding concept, enables the rapid identification of small-molecule inhibitors with high affinity for targets.<sup>63</sup> This approach is especially advantageous for challenging targets such as RdRp, where traditional *in vitro* screening is difficult,

allowing for the swift discovery of lead compounds. In our research, we present novel covalent inhibitors of 3CL<sup>pro</sup> and PL<sup>pro</sup> based on a triazine scaffold and provide the first X-ray crystallographic analysis of the allosteric binding site of PL<sup>pro</sup>. To the best of our knowledge, there are no previously reported covalent inhibitors directly targeting Nsp12. We are the first to reveal non-nucleoside covalent inhibitors with a pyrimidine scaffold against Nsp12 using DEL technology. Furthermore, QM/MM has helped us reveal potential covalent binding sites. Our findings yield valuable insights into the structural basis of viral protease inhibition, laying the groundwork for rational drug design and optimization. By elucidating the precise binding sites and mechanisms of action of our lead compounds, we provide a foundation for the development of more efficacious antiviral inhibitors.

## ASSOCIATED CONTENT

### Supporting Information

The Supporting Information is available free of charge at <https://pubs.acs.org/doi/10.1021/jacs.4c12992>.

Tags code and BBs Smiles data for DEL0C1 ([XLSX](#))

Original screening data for DEL0C1 and DEL0C2 against SARS-CoV-2 PL<sup>pro</sup> ([ZIP](#))

Tags code and BBs Smiles data for DEL0C2 ([XLSX](#))

Original screening data for DEL0C1 and DEL0C2 against SARS-CoV-2 PL<sup>pro</sup> C11S ([ZIP](#))

Original screening data for DEL0C1 and DEL0C2 against SARS-CoV-2 3CL<sup>pro</sup> ([ZIP](#))

Compounds' NMR spectra, HPLC, and HRMS ([ZIP](#))

Synthesis and characterization of inhibitors, X-ray crystal structure details, synthetic procedures and MS spectra of DELs on-DNA compounds, on-DNA covalent selection methods, and enrichment profiles ([PDF](#))

## AUTHOR INFORMATION

### Corresponding Authors

Lianghe Mei – Suzhou Institute of Materia Medica, Suzhou, Jiangsu 215123, P. R. China; Email: [meilianghe@susimm.cn](mailto:meilianghe@susimm.cn)

Hangchen Hu – State Key Laboratory of Drug Research, Shanghai Institute of Materia Medica, Chinese Academy of Sciences, Shanghai 201203, P. R. China; University of Chinese Academy of Sciences, Beijing 100049, P. R. China; School of Pharmaceutical Science and Technology, Hangzhou Institute for Advanced Study, University of Chinese Academy of Sciences, Hangzhou 310024, P. R. China; Email: [201728012342070@simm.ac.cn](mailto:201728012342070@simm.ac.cn)

Xiaojie Lu – State Key Laboratory of Drug Research, Shanghai Institute of Materia Medica, Chinese Academy of Sciences, Shanghai 201203, P. R. China; University of Chinese Academy of Sciences, Beijing 100049, P. R. China; School of Chinese Materia Medica, Nanjing University of Chinese Medicine, Nanjing 210023, P. R. China; [orcid.org/0000-0002-3600-288X](https://orcid.org/0000-0002-3600-288X); Email: [xjlu@simm.ac.cn](mailto:xjlu@simm.ac.cn)

### Authors

Xudong Wang – State Key Laboratory of Drug Research, Shanghai Institute of Materia Medica, Chinese Academy of Sciences, Shanghai 201203, P. R. China; University of Chinese Academy of Sciences, Beijing 100049, P. R. China

Liwei Xiong – School of Pharmaceutical Science and Technology, Hangzhou Institute for Advanced Study, University of Chinese Academy of Sciences, Hangzhou 310024, P. R. China

Ying Zhu – School of Chinese Materia Medica, Nanjing University of Chinese Medicine, Nanjing 210023, P. R. China

Sixiu Liu – State Key Laboratory of Drug Research, Shanghai Institute of Materia Medica, Chinese Academy of Sciences, Shanghai 201203, P. R. China; University of Chinese Academy of Sciences, Beijing 100049, P. R. China

Wenfeng Zhao – State Key Laboratory of Drug Research, Shanghai Institute of Materia Medica, Chinese Academy of Sciences, Shanghai 201203, P. R. China; [orcid.org/0000-0003-2517-4747](https://orcid.org/0000-0003-2517-4747)

Xinyuan Wu – State Key Laboratory of Drug Research, Shanghai Institute of Materia Medica, Chinese Academy of Sciences, Shanghai 201203, P. R. China; University of Chinese Academy of Sciences, Beijing 100049, P. R. China

Mengnisa Seydimemet – School of Chinese Materia Medica, Nanjing University of Chinese Medicine, Nanjing 210023, P. R. China

Linjie Li – State Key Laboratory of Drug Research, Shanghai Institute of Materia Medica, Chinese Academy of Sciences, Shanghai 201203, P. R. China; [orcid.org/0000-0002-9817-1793](https://orcid.org/0000-0002-9817-1793)

Peiqi Ding – School of Pharmaceutical Science and Technology, Hangzhou Institute for Advanced Study, University of Chinese Academy of Sciences, Hangzhou 310024, P. R. China

Xian Lin – Suzhou Institute of Materia Medica, Suzhou, Jiangsu 215123, P. R. China

Jiaxiang Liu – State Key Laboratory of Drug Research, Shanghai Institute of Materia Medica, Chinese Academy of Sciences, Shanghai 201203, P. R. China

Xuan Wang – State Key Laboratory of Drug Research, Shanghai Institute of Materia Medica, Chinese Academy of Sciences, Shanghai 201203, P. R. China

Zhiqiang Duan – State Key Laboratory of Drug Research, Shanghai Institute of Materia Medica, Chinese Academy of Sciences, Shanghai 201203, P. R. China

Weiwei Lu – State Key Laboratory of Drug Research, Shanghai Institute of Materia Medica, Chinese Academy of Sciences, Shanghai 201203, P. R. China

Yanrui Suo – State Key Laboratory of Drug Research, Shanghai Institute of Materia Medica, Chinese Academy of Sciences, Shanghai 201203, P. R. China; University of Chinese Academy of Sciences, Beijing 100049, P. R. China

Mengqing Cui – State Key Laboratory of Drug Research, Shanghai Institute of Materia Medica, Chinese Academy of Sciences, Shanghai 201203, P. R. China

Jinfeng Yue – State Key Laboratory of Drug Research, Shanghai Institute of Materia Medica, Chinese Academy of Sciences, Shanghai 201203, P. R. China

Rui Jin – State Key Laboratory of Drug Research, Shanghai Institute of Materia Medica, Chinese Academy of Sciences, Shanghai 201203, P. R. China

Mingyue Zheng – State Key Laboratory of Drug Research, Shanghai Institute of Materia Medica, Chinese Academy of Sciences, Shanghai 201203, P. R. China; University of Chinese Academy of Sciences, Beijing 100049, P. R. China; [orcid.org/0000-0002-3323-3092](https://orcid.org/0000-0002-3323-3092)

Yechun Xu – State Key Laboratory of Drug Research, Shanghai Institute of Materia Medica, Chinese Academy of

Sciences, Shanghai 201203, P. R. China; University of Chinese Academy of Sciences, Beijing 100049, P. R. China; School of Chinese Materia Medica, Nanjing University of Chinese Medicine, Nanjing 210023, P. R. China; School of Pharmaceutical Science and Technology, Hangzhou Institute for Advanced Study, University of Chinese Academy of Sciences, Hangzhou 310024, P. R. China; [orcid.org/0000-0002-1581-6155](https://orcid.org/0000-0002-1581-6155)

Complete contact information is available at:  
<https://pubs.acs.org/10.1021/jacs.4c12992>

## Author Contributions

#X.W., L.X., Y.Z., and S.L. contributed equally.

## Notes

The authors declare the following competing financial interest(s): X.L., Y.X., and X.W. have submitted three patents application on the compounds. Crystal structures have been deposited in the PDB.

## ACKNOWLEDGMENTS

X.L. was supported by the National Natural Science Foundation of China (NSFC) 22377139, 92253305. H.H. gratefully appreciates the National Natural Science Foundation of China (NSFC) 32301050 for the support of this work. This work was also supported in part by the Strategic Priority Research Program of the Chinese Academy of Sciences (Grant No. XDB0490000 to Y.X.), Shanghai Action Plan for Science, Technology and Innovation (23HC1401200), Shanghai Institute of Pharmaceutical Sciences independent research projects (SIMM0220233001), and State Key Laboratory of Drug Research (SKLDR-2022-LH-01).

## REFERENCES

- (1) Zhu, N.; Zhang, D.; Wang, W.; Li, X.; Yang, B.; Song, J.; Zhao, X.; Huang, B.; Shi, W.; Lu, R.; Niu, P.; Zhan, F.; Ma, X.; Wang, D.; Xu, W.; Wu, G.; Gao, G. F.; Tan, W. A Novel Coronavirus from Patients with Pneumonia in China, 2019. *N. Engl. J. Med.* **2020**, *382*, 727–733.
- (2) Zhang, L.; Li, Q.; Liang, Z.; Li, T.; Liu, S.; Cui, Q.; Nie, J.; Wu, Q.; Qu, X.; Huang, W.; Wang, Y. The significant immune escape of pseudotyped SARS-CoV-2 variant Omicron. *Emerg. Microb. Infect.* **2022**, *11*, 1–5.
- (3) Iketani, S.; Mohri, H.; Culbertson, B.; Hong, S. J.; Duan, Y.; Luck, M. I.; Annavajhala, M. K.; Guo, Y.; Sheng, Z.; Uhlemann, A.-C.; Goff, S. P.; Sabo, Y.; Yang, H.; Chavez, A.; Ho, D. D. Multiple pathways for SARS-CoV-2 resistance to nirmatrelvir. *Nature* **2023**, *613*, 558–564.
- (4) Hu, Y.; Lewandowski, E. M.; Tan, H.; Zhang, X.; Morgan, R. T.; Zhang, X.; Jacobs, L. M. C.; Butler, S. G.; Gongora, M. V.; Choy, J.; Deng, X.; Chen, Y.; Wang, J. Naturally Occurring Mutations of SARS-CoV-2 Main Protease Confer Drug Resistance to Nirmatrelvir. *ACS Cent. Sci.* **2023**, *9*, 1658–1669.
- (5) Stevens, L. J.; Pruijssers, A. J.; Lee, H. W.; Gordon, C. J.; Tchesnokov, E. P.; Gribble, J.; George, A. S.; Hughes, T. M.; Lu, X.; Li, J.; Perry, J. K.; Porter, D. P.; Cihlar, T.; Sheahan, T. P.; Baric, R. S.; Götte, M.; Denison, M. R. Mutations in the SARS-CoV-2 RNA-dependent RNA polymerase confer resistance to remdesivir by distinct mechanisms. *Sci. Transl. Med.* **2022**, *14*, No. eab0718.
- (6) Sjaarda, C. P.; Lau, L.; Simpson, J. T.; Fattouh, R.; Biondi, M. J.; Maguire, F.; Campigotto, A.; Feng, Y.; Tozer, K.; Wong, H.; Sung, W. W. L.; Kim, S.; Marshall, C. R.; Sheth, P. M.; Kozak, R. Prevalence of Low-Frequency, Antiviral Resistance Variants in SARS-CoV-2 Isolates in Ontario, Canada, 2020–2023. *JAMA Netw. Open* **2023**, *6*, No. e2324963.
- (7) Hirotsu, Y.; Kobayashi, H.; Kakizaki, Y.; Saito, A.; Tsutsui, T.; Kawaguchi, M.; Shimamura, S.; Hata, K.; Hanawa, S.; Toyama, J.; Miyashita, Y.; Omata, M. Multidrug-resistant mutations to antiviral and antibody therapy in an immunocompromised patient infected with SARS-CoV-2. *Med* **2023**, *4*, 813–824.e4.
- (8) Zhou, P.; Yang, X.-L.; Wang, X.-G.; Hu, B.; Zhang, L.; Zhang, W.; Si, H.-R.; Zhu, Y.; Li, B.; Huang, C.-L.; Chen, H.-D.; Chen, J.; Luo, Y.; Guo, H.; Jiang, R.-D.; Liu, M.-Q.; Chen, Y.; Shen, X.-R.; Wang, X.; Zheng, X.-S.; Zhao, K.; Chen, Q.-J.; Deng, F.; Liu, L.-L.; Yan, B.; Zhan, F.-X.; Wang, Y.-Y.; Xiao, G.-F.; Shi, Z.-L. A pneumonia outbreak associated with a new coronavirus of probable bat origin. *Nature* **2020**, *579*, 270–273.
- (9) Walls, A. C.; Park, Y.-J.; Tortorici, M. A.; Wall, A.; McGuire, A. T.; Veesler, D. Structure, Function, and Antigenicity of the SARS-CoV-2 Spike Glycoprotein. *Cell* **2020**, *181*, 281–292.e6.
- (10) Dhama, K.; Khan, S.; Tiwari, R.; Sircar, S.; Bhat, S.; Malik, Y.; Singh, K.; Chaicumpa, W.; Bonilla-Aldana, D.; Rodriguez-Morales, A. Coronavirus Disease 2019–COVID-19. *Clin. Microbiol. Rev.* **2020**, *33*, No. e00028-20.
- (11) Rota, P. A.; Oberste, M. S.; Monroe, S. S.; Nix, W. A.; Campagnoli, R.; Icenogle, J. P.; Peñaranda, S.; Bankamp, B.; Maher, K.; Chen, M. h.; Tong, S.; Tamin, A.; Lowe, L.; Frace, M.; DeRisi, J. L.; Chen, Q.; Wang, D.; Erdman, D. D.; Peret, T. C. T.; Burns, C.; Ksiazek, T. G.; Rollin, P. E.; Sanchez, A.; Liffick, S.; Holloway, B.; Limor, J.; McCaustland, K.; Olsen-Rasmussen, M.; Fouchier, R.; Günther, S.; Osterhaus, A. D. M. E.; Drosten, C.; Pallansch, M. A.; Anderson, L. J.; Bellini, W. J. Characterization of a Novel Coronavirus Associated with Severe Acute Respiratory Syndrome. *Science* **2003**, *300*, 1394–1399.
- (12) Assiri, A.; McGeer, A.; Perl, T. M.; Price, C. S.; Al Rabeeah, A. A.; Cummings, D. A. T.; Alabdullatif, Z. N.; Assad, M.; Almulhim, A.; Makhdoom, H.; Madani, H.; Alhakeem, R.; Al-Tawfiq, J. A.; Cotten, M.; Watson, S. J.; Kellam, P.; Zumla, A. I.; Memish, Z. A. Hospital Outbreak of Middle East Respiratory Syndrome Coronavirus. *N. Engl. J. Med.* **2013**, *369*, 407–416.
- (13) Zumla, A.; Hui, D. S.; Perlman, S. Middle East respiratory syndrome. *Lancet* **2015**, *386*, 995–1007.
- (14) Anirudhan, V.; Lee, H.; Cheng, H.; Cooper, L.; Rong, L. Targeting SARS-CoV-2 viral proteases as a therapeutic strategy to treat COVID-19. *J. Med. Virol.* **2021**, *93*, 2722–2734.
- (15) Mousaqil, M.; Ollivier, E.; Chiu, H.-P.; Van Tol, S.; Rudolphi-Soto, P.; Stevens, C.; Bhumkar, A.; Hunter, D. J. B.; Freiberg, A. N.; Jacques, D.; Lee, B.; Sierecki, E.; Gambin, Y. SARS-CoV-2 proteases PLpro and 3CLpro cleave IRF3 and critical modulators of inflammatory pathways (NLRP12 and TAB1): implications for disease presentation across species. *Emerg. Microb. Infect.* **2021**, *10*, 178–195.
- (16) Thiel, V.; Ivanov, K. A.; Putics, A.; Hertzog, T.; Schelle, B.; Bayer, S.; Weißbrich, B.; Snijder, E. J.; Rabenau, H.; Doerr, H. W.; Gorbalyena, A. E.; Ziebuhr, J. Mechanisms and enzymes involved in SARS coronavirus genome expression. *J. Gen. Virol.* **2003**, *84*, 2305–2315.
- (17) Anand, K.; Ziebuhr, J.; Wadhwani, P.; Mesters, J. R.; Hilgenfeld, R. Coronavirus Main Proteinase (3CLpro) Structure: Basis for Design of Anti-SARS Drugs. *Science* **2003**, *300*, 1763–1767.
- (18) Jin, Z.; Du, X.; Xu, Y.; Deng, Y.; Liu, M.; Zhao, Y.; Zhang, B.; Li, X.; Zhang, L.; Peng, C.; Duan, Y.; Yu, J.; Wang, L.; Yang, K.; Liu, F.; Jiang, R.; Yang, X.; You, T.; Liu, X.; Yang, X.; Bai, F.; Liu, H.; Liu, X.; Guddat, L. W.; Xu, W.; Xiao, G.; Qin, C.; Shi, Z.; Jiang, H.; Rao, Z.; Yang, H. Structure of Mpro from SARS-CoV-2 and discovery of its inhibitors. *Nature* **2020**, *582*, 289–293.
- (19) Zhang, L.; Lin, D.; Sun, X.; Curth, U.; Drosten, C.; Sauerhering, L.; Becker, S.; Rox, K.; Hilgenfeld, R. Crystal structure of SARS-CoV-2 main protease provides a basis for design of improved  $\alpha$ -ketoamide inhibitors. *Science* **2020**, *368*, 409–412.
- (20) Báez-Santos, Y. M.; St John, S. E.; Mesecar, A. D. The SARS-coronavirus papain-like protease: Structure, function and inhibition by designed antiviral compounds. *Antiviral Res.* **2015**, *115*, 21–38.

- (21) Shin, D.; Mukherjee, R.; Grewe, D.; Bojkova, D.; Baek, K.; Bhattacharya, A.; Schulz, L.; Widera, M.; Mehdipour, A. R.; Tascher, G.; Geurink, P. P.; Wilhelm, A.; van der Heden van Noort, G. J.; Ovaa, H.; Müller, S.; Knobeloch, K.-P.; Rajalingam, K.; Schulman, B. A.; Cinatl, J.; Hummer, G.; Ciesek, S.; Dikic, I. Papain-like protease regulates SARS-CoV-2 viral spread and innate immunity. *Nature* **2020**, *587*, 657–662.
- (22) Gao, X.; Qin, B.; Chen, P.; Zhu, K.; Hou, P.; Wojdyla, J. A.; Wang, M.; Cui, S. Crystal structure of SARS-CoV-2 papain-like protease. *Acta Pharm. Sin. B* **2021**, *11*, 237–245.
- (23) Gao, Y.; Yan, L.; Huang, Y.; Liu, F.; Zhao, Y.; Cao, L.; Wang, T.; Sun, Q.; Ming, Z.; Zhang, L.; Ge, J.; Zheng, L.; Zhang, Y.; Wang, H.; Zhu, Y.; Zhu, C.; Hu, T.; Hua, T.; Zhang, B.; Yang, X.; Li, J.; Yang, H.; Liu, Z.; Xu, W.; Guddat, L. W.; Wang, Q.; Lou, Z.; Rao, Z. Structure of the RNA-dependent RNA polymerase from COVID-19 virus. *Science* **2020**, *368*, 779–782.
- (24) Yin, W.; Mao, C.; Luan, X.; Shen, D.-D.; Shen, Q.; Su, H.; Wang, X.; Zhou, F.; Zhao, W.; Gao, M.; Chang, S.; Xie, Y.-C.; Tian, G.; Jiang, H.-W.; Tao, S.-C.; Shen, J.; Jiang, Y.; Jiang, H.; Xu, Y.; Zhang, S.; Zhang, Y.; Xu, H. E. Structural basis for inhibition of the RNA-dependent RNA polymerase from SARS-CoV-2 by remdesivir. *Science* **2020**, *368*, 1499–1504.
- (25) Dai, W.; Zhang, B.; Jiang, X. M.; Su, H.; Li, J.; Zhao, Y.; Xie, X.; Jin, Z.; Peng, J.; Liu, F.; Li, C.; Li, Y.; Bai, F.; Wang, H.; Cheng, X.; Cen, X.; Hu, S.; Yang, X.; Wang, J.; Liu, X.; Xiao, G.; Jiang, H.; Rao, Z.; Zhang, L. K.; Xu, Y.; Yang, H.; Liu, H. Structure-based design of antiviral drug candidates targeting the SARS-CoV-2 main protease. *Science* **2020**, *368*, 1331–1335.
- (26) Dampalla, C. S.; Kim, Y.; Bickmeier, N.; Rathnayake, A. D.; Nguyen, H. N.; Zheng, J.; Kashipathy, M. M.; Baird, M. A.; Battaile, K. P.; Lovell, S.; Perlman, S.; Chang, K.-O.; Groutas, W. C. Structure-Guided Design of Conformationally Constrained Cyclohexane Inhibitors of Severe Acute Respiratory Syndrome Coronavirus-2 3CL Protease. *J. Med. Chem.* **2021**, *64*, 10047–10058.
- (27) Brogi, S.; Ibba, R.; Rossi, S.; Butini, S.; Calderone, V.; Gemma, S.; Campiani, G. Covalent Reversible Inhibitors of Cysteine Proteases Containing the Nitrile Warhead: Recent Advancement in the Field of Viral and Parasitic Diseases. *Molecules* **2022**, *27*, 2561–2575.
- (28) Bai, B.; Belovodskiy, A.; Hena, M.; Kandadai, A. S.; Joyce, M. A.; Saffran, H. A.; Shields, J. A.; Khan, M. B.; Arutyunova, E.; Lu, J.; Bajwa, S. K.; Hockman, D.; Fischer, C.; Lamer, T.; Vuong, W.; van Belkum, M. J.; Gu, Z.; Lin, F.; Du, Y.; Xu, J.; Rahim, M.; Young, H. S.; Vederas, J. C.; Tyrrell, D. L.; Lemieux, M. J.; Nieman, J. A. Peptidomimetic  $\alpha$ -Acyloxymethylketone Warheads with Six-Membered Lactam P1 Glutamine Mimic: SARS-CoV-2 3CL Protease Inhibition, Coronavirus Antiviral Activity, and in Vitro Biological Stability. *J. Med. Chem.* **2022**, *65*, 2905–2925.
- (29) Konno, S.; Kobayashi, K.; Senda, M.; Funai, Y.; Seki, Y.; Tamai, I.; Schäkel, L.; Sakata, K.; Pillaiyar, T.; Taguchi, A.; Taniguchi, A.; Güttschow, M.; Müller, C. E.; Takeuchi, K.; Hirohama, M.; Kawaguchi, A.; Kojima, M.; Senda, T.; Shirasaki, Y.; Kamitani, W.; Hayashi, Y. 3CL Protease Inhibitors with an Electrophilic Arylketone Moiety as Anti-SARS-CoV-2 Agents. *J. Med. Chem.* **2022**, *65*, 2926–2939.
- (30) Mandadapu, S. R.; Gunnam, M. R.; Tiew, K.-C.; Uy, R. A. Z.; Prior, A. M.; Alliston, K. R.; Hua, D. H.; Kim, Y.; Chang, K.-O.; Groutas, W. C. Inhibition of norovirus 3CL protease by bisulfite adducts of transition state inhibitors. *Bioorg. Med. Chem. Lett.* **2013**, *23*, 62–65.
- (31) Saravoltz, L. D.; Depcinski, S.; Sharma, M. Molnupiravir and Nirmatrelvir-Ritonavir: Oral Coronavirus Disease 2019 Antiviral Drugs. *Clin. Infect. Dis.* **2023**, *76*, 165–171.
- (32) Wang, X.; Zhu, Y.; Zhao, Q.; Lu, W.; Xu, Y.; Hu, H.; Lu, X. Chemical Space Profiling of SARS-CoV-2 PLpro Using DNA-Encoded Focused Libraries. *ACS Med. Chem. Lett.* **2024**, *15*, 555–564.
- (33) Shen, Z.; Ratia, K.; Cooper, L.; Kong, D.; Lee, H.; Kwon, Y.; Li, Y.; Alqarni, S.; Huang, F.; Dubrovsky, O.; Rong, L.; Thatcher, G. R. J.; Xiong, R. Design of SARS-CoV-2 PLpro Inhibitors for COVID-19 Antiviral Therapy Leveraging Binding Cooperativity. *J. Med. Chem.* **2022**, *65*, 2940–2955.
- (34) Shan, H.; Liu, J.; Shen, J.; Dai, J.; Xu, G.; Lu, K.; Han, C.; Wang, Y.; Xu, X.; Tong, Y.; Xiang, H.; Ai, Z.; Zhuang, G.; Hu, J.; Zhang, Z.; Li, Y.; Pan, L.; Tan, L. Development of potent and selective inhibitors targeting the papain-like protease of SARS-CoV-2. *Cell Chem. Biol.* **2021**, *28*, 855–865.e9.
- (35) Ma, C.; Sacco, M. D.; Xia, Z.; Lambrinidis, G.; Townsend, J. A.; Hu, Y.; Meng, X.; Szeto, T.; Ba, M.; Zhang, X.; Gongora, M.; Zhang, F.; Marty, M. T.; Xiang, Y.; Kolocouris, A.; Chen, Y.; Wang, J. Discovery of SARS-CoV-2 Papain-like Protease Inhibitors through a Combination of High-Throughput Screening and a FlipGFP-Based Reporter Assay. *ACS Cent. Sci.* **2021**, *7*, 1245–1260.
- (36) Tan, B.; Zhang, X.; Ansari, A.; Jadhav, P.; Tan, H.; Li, K.; Chopra, A.; Ford, A.; Chi, X.; Ruiz, F. X.; Arnold, E.; Deng, X.; Wang, J. Design of a SARS-CoV-2 papain-like protease inhibitor with antiviral efficacy in a mouse model. *Science* **2024**, *383*, 1434–1440.
- (37) Sanders, B. C.; Pokhrel, S.; Labbe, A. D.; Mathews, I. I.; Cooper, C. J.; Davidson, R. B.; Phillips, G.; Weiss, K. L.; Zhang, Q.; O'Neill, H.; Kaur, M.; Schmid, J. G.; Reichard, W.; Surendranathan, S.; Parvathareddy, J.; Phillips, L.; Rainville, C.; Stern, D. E.; Kumar, D.; Andi, B.; Babnigg, G.; Moriarty, N. W.; Adams, P. D.; Joachimiak, A.; Hurst, B. L.; Kumar, S.; Butt, T. R.; Jonsson, C. B.; Ferrins, L.; Wakatsuki, S.; Galanis, S.; Head, M. S.; Parks, J. M. Potent and selective covalent inhibition of the papain-like protease from SARS-CoV-2. *Nat. Commun.* **2023**, *14*, 1733–1749.
- (38) Bekheit, M. S.; Panda, S. S.; Grgis, A. S. Potential RNA-dependent RNA polymerase (RdRp) inhibitors as prospective drug candidates for SARS-CoV-2. *Eur. J. Med. Chem.* **2023**, *252*, 115292–115312.
- (39) Shehzadi, K.; Saba, A.; Yu, M.; Liang, J. Structure-Based Drug Design of RdRp Inhibitors against SARS-CoV-2. *Top. Curr. Chem.* **2023**, *381*, 22–75.
- (40) Ding, Y.; Belyanskaya, S.; DeLorey, J. L.; Messer, J. A.; Joseph Franklin, G.; Centrella, P. A.; Morgan, B. A.; Clark, M. A.; Skinner, S. R.; Dodson, J. W.; Li, P.; Marino, J. P.; Israel, D. I. Discovery of soluble epoxide hydrolase inhibitors through DNA-encoded library technology (ELT). *Bioorg. Med. Chem.* **2021**, *41*, 116216–116225.
- (41) Li, L.; Su, M.; Lu, W.; Song, H.; Liu, J.; Wen, X.; Suo, Y.; Qi, J.; Luo, X.; Zhou, Y.-B.; Liao, X.-H.; Li, J.; Lu, X. Triazine-Based Covalent DNA-Encoded Libraries for Discovery of Covalent Inhibitors of Target Proteins. *ACS Med. Chem. Lett.* **2022**, *13*, 1574–1581.
- (42) Taylor, D. M.; Anglin, J.; Park, S.; Ucisik, M. N.; Faver, J. C.; Simmons, N.; Jin, Z.; Palaniappan, M.; Nyshadham, P.; Li, F.; Campbell, J.; Hu, L.; Sankaran, B.; Prasad, B. V. V.; Huang, H.; Matzuk, M. M.; Palzkill, T. Identifying Oxacillinase-48 Carbapenemase Inhibitors Using DNA-Encoded Chemical Libraries. *ACS Infect. Dis.* **2020**, *6*, 1214–1227.
- (43) Ding, Y.; O'Keefe, H.; DeLorey, J. L.; Israel, D. I.; Messer, J. A.; Chiu, C. H.; Skinner, S. R.; Matico, R. E.; Murray-Thompson, M. F.; Li, F.; Clark, M. A.; Cuozzo, J. W.; Arico-Muendel, C.; Morgan, B. A. Discovery of Potent and Selective Inhibitors for ADAMTS-4 through DNA-Encoded Library Technology (ELT). *ACS Med. Chem. Lett.* **2015**, *6*, 888–893.
- (44) Goodnow, R. A.; Dumelin, C. E.; Keefe, A. D. DNA-encoded chemistry: enabling the deeper sampling of chemical space. *Nat. Rev. Drug Discovery* **2017**, *16*, 131–147.
- (45) Mason, J. W.; Chow, Y. T.; Hudson, L.; Tutter, A.; Michaud, G.; Westphal, M. V.; Shu, W.; Ma, X.; Tan, Z. Y.; Coley, C. W.; Clemons, P. A.; Bonazzi, S.; Berst, F.; Briner, K.; Liu, S.; Zécri, F. J.; Schreiber, S. L. DNA-encoded library-enabled discovery of proximity-inducing small molecules. *Nat. Chem. Biol.* **2024**, *20*, 170–179.
- (46) Zhou, Y.; Shen, W.; Gao, Y.; Peng, J.; Li, Q.; Wei, X.; Liu, S.; Lam, F. S.; Mayol-Llinàs, J.; Zhao, G.; Li, G.; Li, Y.; Sun, H.; Cao, Y.; Li, X. Protein-templated ligand discovery via the selection of DNA-encoded dynamic libraries. *Nat. Chem.* **2024**, *16*, 543–555.
- (47) Oehler, S.; Lucaroni, L.; Migliorini, F.; Elsayed, A.; Prati, L.; Puglioli, S.; Matasci, M.; Schirà, K.; Scheuermann, J.; Yudin, D.; Jia,

- M.; Ban, N.; Bushnell, D.; Kornberg, R.; Cazzamalli, S.; Neri, D.; Favalli, N.; Bassi, G. A DNA-encoded chemical library based on chiral 4-amino-proline enables stereospecific isozyme-selective protein recognition. *Nat. Chem.* **2023**, *15*, 1431–1443.
- (48) Hu, H.; Wang, Q.; Su, H.; Shao, Q.; Zhao, W.; Chen, G.; Li, M.; Xu, Y. Identification of Cysteine 270 as a Novel Site for Allosteric Modulators of SARS-CoV-2 Papain-Like Protease\*\*. *Angew. Chem., Int. Ed.* **2022**, *61*, No. e20221237.
- (49) Shao, Q.; Xiong, M.; Li, J.; Hu, H.; Su, H.; Xu, Y. Unraveling the catalytic mechanism of SARS-CoV-2 papain-like protease with allosteric modulation of C270 mutation using multiscale computational approaches. *Chem. Sci.* **2023**, *14*, 4681–4696.
- (50) Amblard, F.; LeCher, J. C.; De, R.; Zhou, S.; Liu, P.; Goh, S. L.; Tao, S.; Patel, D.; Downs-Bowen, J.; Zandi, K.; Zhang, H.; Chaudhry, G.; McBrayer, T.; Muczynski, M.; Al-Homoudi, A.; Engel, J.; Lan, S.; Sarafianos, S. G.; Kovari, L. C.; Schinazi, R. F. Synthesis and biological evaluation of novel peptidomimetic inhibitors of the coronavirus 3C-like protease. *Eur. J. Med. Chem.* **2024**, *268*, 116263–116282.
- (51) Zhang, F.-M.; Huang, T.; Wang, F.; Zhang, G.-S.; Liu, D.; Dai, J.; Zhang, J.-W.; Li, Q.-H.; Lin, G.-Q.; Gao, D.; Zhao, J.; Tian, P. Discovery of highly potent covalent SARS-CoV-2 3CLpro inhibitors bearing 2-sulfoxy-1,3,4-oxadiazole scaffold for combating COVID-19. *Eur. J. Med. Chem.* **2023**, *260*, 115721–115738.
- (52) Wang, R.; Chen, X.; Li, H.; Chen, X.; Sun, D.; Yu, D.; Lu, J.; Xie, Y.; Zhang, Q.; Xu, J.; Zhang, W.; Chen, H.; Liu, S.; Chen, L. Danshensu inhibits SARS-CoV-2 by targeting its main protease as a specific covalent inhibitor and discovery of bifunctional compounds eliciting antiviral and anti-inflammatory activity. *Int. J. Biol. Macromol.* **2024**, *257*, 128623–128640.
- (53) Zhu, M.; Fu, T.; You, M.; Cao, J.; Yang, H.; Chen, X.; Zhang, Q.; Xu, Y.; Jiang, X.; Zhang, L.; Su, H.; Zhang, Y.; Shen, J. Design, synthesis and biological evaluation of covalent peptidomimetic 3CL protease inhibitors containing nitrile moiety. *Bioorg. Med. Chem.* **2023**, *87*, 117316–117328.
- (54) Pillaiyar, T.; Flury, P.; Krüger, N.; Su, H.; Schäkel, L.; Barbosa Da Silva, E.; Eppler, O.; Kronenberger, T.; Nie, T.; Luedtke, S.; Rocha, C.; Sylvester, K.; Petry, M. R. I.; McKerrow, J. H.; Poso, A.; Pöhlmann, S.; Gütschow, M.; O'Donoghue, A. J.; Xu, Y.; Müller, C. E.; Laufer, S. A. Small-Molecule Thioesters as SARS-CoV-2 Main Protease Inhibitors: Enzyme Inhibition, Structure–Activity Relationships, Antiviral Activity, and X-ray Structure Determination. *J. Med. Chem.* **2022**, *65*, 9376–9395.
- (55) Wang, Q.; Wu, J.; Wang, H.; Gao, Y.; Liu, Q.; Mu, A.; Ji, W.; Yan, L.; Zhu, Y.; Zhu, C.; Fang, X.; Yang, X.; Huang, Y.; Gao, H.; Liu, F.; Ge, J.; Sun, Q.; Yang, X.; Xu, W.; Liu, Z.; Yang, H.; Lou, Z.; Jiang, B.; Guddat, L. W.; Gong, P.; Rao, Z. Structural Basis for RNA Replication by the SARS-CoV-2 Polymerase. *Cell* **2020**, *182*, 417–428.e13.
- (56) Awoonor-Williams, E.; Golosov, A. A.; Hornak, V. Benchmarking In Silico Tools for Cysteine pKa Prediction. *J. Chem. Inf. Model.* **2023**, *63*, 2170–2180.
- (57) Gao, S.; Song, L.; Xu, H.; Fikatas, A.; Oeyen, M.; De Jonghe, S.; Zhao, F.; Jing, L.; Jochmans, D.; Vangeel, L.; Cheng, Y.; Kang, D.; Neyts, J.; Herdewijn, P.; Schols, D.; Zhan, P.; Liu, X. Identification of Polyphenol Derivatives as Novel SARS-CoV-2 and DENV Non-Nucleoside RdRp Inhibitors. *Molecules* **2022**, *28*, 160–175.
- (58) Chaube, U.; Patel, B. D.; Bhatt, H. G. A hypothesis on designing strategy of effective RdRp inhibitors for the treatment of SARS-CoV-2. *3 Biotech* **2022**, *13*, 12–21.
- (59) Cao, B.; Wang, Y.; Lu, H.; Huang, C.; Yang, Y.; Shang, L.; Chen, Z.; Jiang, R.; Liu, Y.; Lin, L.; Peng, P.; Wang, F.; Gong, F.; Hu, H.; Cheng, C.; Yao, X.; Ye, X.; Zhou, H.; Shen, Y.; Liu, C.; Wang, C.; Yi, Z.; Hu, B.; Xu, J.; Gu, X.; Shen, J.; Xu, Y.; Zhang, L.; Fan, J.; Tang, R.; Wang, C. Oral Simnotrelvir for Adult Patients with Mild-to-Moderate Covid-19. *N. Engl. J. Med.* **2024**, *390*, 230–241.
- (60) Hammond, J.; Leister-Tebbe, H.; Gardner, A.; Abreu, P.; Bao, W.; Wisemandle, W.; Baniecki, M.; Hendrick, V. M.; Damle, B.; Simón-Campos, A.; Pypstra, R.; Rusnak, J. M. Oral Nirmatrelvir for High-Risk, Nonhospitalized Adults with Covid-19. *N. Engl. J. Med.* **2022**, *386*, 1397–1408.
- (61) Cao, Z.; Gao, W.; Bao, H.; Feng, H.; Mei, S.; Chen, P.; Gao, Y.; Cui, Z.; Zhang, Q.; Meng, X.; Gui, H.; Wang, W.; Jiang, Y.; Song, Z.; Shi, Y.; Sun, J.; Zhang, Y.; Xie, Q.; Xu, Y.; Ning, G.; Gao, Y.; Zhao, R. VV116 versus Nirmatrelvir–Ritonavir for Oral Treatment of Covid-19. *N. Engl. J. Med.* **2023**, *388*, 406–417.
- (62) Beigel, J. H.; Tomashek, K. M.; Dodd, L. E.; Mehta, A. K.; Zingman, B. S.; Kalil, A. C.; Hohmann, E.; Chu, H. Y.; Luetkemeyer, A.; Kline, S.; Lopez de Castilla, D.; Finberg, R. W.; Dierberg, K.; Tapson, V.; Hsieh, L.; Patterson, T. F.; Paredes, R.; Sweeney, D. A.; Short, W. R.; Touloumi, G.; Lye, D. C.; Ohmagari, N.; Oh, M.-d.; Ruiz-Palacios, G. M.; Benfield, T.; Fätkenheuer, G.; Kortepeter, M. G.; Atmar, R. L.; Creech, C. B.; Lundgren, J.; Babiker, A. G.; Pett, S.; Neaton, J. D.; Burgess, T. H.; Bonnett, T.; Green, M.; Makowski, M.; Osinusi, A.; Nayak, S.; Lane, H. C. Remdesivir for the Treatment of Covid-19—Final Report. *N. Engl. J. Med.* **2020**, *383*, 1813–1826.
- (63) Dickson, P. DNA-Encoded Library Technology—A Catalyst for Covalent Ligand Discovery. *ACS Chem. Biol.* **2024**, *19*, 802–808.